

SUPPORTING INFORMATION

2D to 3D crossover of the magnetic properties in ordered arrays of iron oxide nanocrystals

Bertrand Faure, Erik Wetterskog, Klas Gunnarsson, Elisabeth Josten, Raphaël P.
Hermann, Thomas Brückel, Jens Wenzel Andreasen, Florian Meneau, Mathias
Meyer, Alexander Lyubartsev, Lennart Bergström, German Salazar-Alvarez, and
Peter Svedlindh*

E-mail: peter.svedlindh@angstrom.uu.se

*To whom correspondence should be addressed

Contents

1	Sample preparation	3
1.1	Synthesis and dispersion of the nanoparticles	3
1.2	Substrate cleaning and particle deposition	3
2	Characterization of the nanoparticles	4
2.1	Powder X-ray diffraction	4
2.2	Transmission electron microscopy	5
2.3	Small angle X-ray scattering	6
2.4	Dynamic light scattering	6
3	Characterization of the arrays	7
3.1	GISAXS characterization of the arrays	7
3.2	AFM characterization of the arrays	7
4	Magnetic characterization	9
4.1	Magnetic relaxation time	9
4.2	Temperature dependence of the magnetization	11
4.3	Temperature dependence of the susceptibility	12
4.4	Exchange bias effect	13
4.5	Full hysteresis loops	13
4.6	AC susceptibility measurements	14
4.7	Array thickness dependence of the non-equilibrium behavior	16
4.8	Onset of the non-equilibrium state	17
5	Monte Carlo simulations	18
5.1	Description of the model system	18
5.2	Observation of the 2D to 3D crossover	21
5.3	Field-dependent susceptibility	22

1 Sample preparation

1.1 Synthesis and dispersion of the nanoparticles

Sodium oleate (NaOl, 82%), oleic acid (OIA, 90%), 1-octadecene (OD, 90%) and $\text{FeCl}_3 \cdot 6\text{H}_2\text{O}$ (97%) were purchased from Sigma-Aldrich and used as received.

The iron (III) oleate precursor was prepared by refluxing 10.8 g of iron chloride (40 mmol) with 36.5 g NaOl in a solvent mixture of 140 mL n-hexane, 80 mL ethanol and 60 mL water at 70°C for 1 h. The organic layer was separated, washed 3 times with 30 mL distilled water, and dried in a rotary evaporator. The iron (III) oleate was dissolved in 200 mL OD at 50°C under vacuum. The solution was then degassed at 90°C under vacuum for 90 min. The main synthesis setup was thoroughly cleaned and dried by connecting the hot glassware to a stream of dry N_2 to remove atmospheric moisture. OIA (5.7 g, 6.42 mL) was added to the reaction flask and the mixture was then brought to reflux at 320°C under a constant heating rate of 2.6°C/min, held for 30 min, and removed from heating.

The particles were separated from the mother liquor into a thick paste by repeated flocculation-redisersion cycles. In a typical cycle, the iron oxide precipitate was dispersed in few mL of n-hexane or n-heptane, sonicated, and flocculated upon the addition of a 1:1 ethanol/acetone mixture. The dispersion in cyclohexane (0.1 wt% inorganic content) was prepared from a Fe_2O_3 :OIA:cyclohexane mixture (1:20:1000 by weight) and sonicated for 2.5 h. The sonication was followed by filtration through a 0.2 μm syringe filter. The dispersion was centrifuged at 30000 g for 15 min and the precipitate was discarded.

1.2 Substrate cleaning and particle deposition

Organic and particulate contaminants were removed from the pre-diced silicon wafers (Ted Pella Inc, (111) surfaces, $5 \times 5 \text{ mm}^2$) by cleaning. The cleaning steps involved immersing the wafers in a $\text{NH}_4\text{OH}:\text{H}_2\text{O}_2:\text{H}_2\text{O}$ 1:1:6 solution at 70°C for 15 min, followed by rinsing with deionized water and immersion into a fresh $\text{HCl}:\text{H}_2\text{O}_2:\text{H}_2\text{O}$, 1:1:6 solution at 70°C for 10 min. The wafers were

finally rinsed in running deionized water for 10 min, and then dried at 100°C for 1 h.

The nanoparticle paste was dispersed in toluene under sonication to make a concentrated stock dispersion. The dispersion was further diluted into 3 dispersions with concentrations of 0.050, 0.125 and 0.625 mg/mL of γ -Fe₂O₃. 20 μ L droplets from each dispersion were deposited on the cleaned silicon wafers and placed in a solvent saturated compartment. The droplet evaporation step was carried out by placing a stack of filter paper soaked in toluene inside the chamber, and thereafter allowing the entire experimental chamber to dry out slowly for 1-3 days. A magnetic field of 35 mT (27.9 kA/m) was applied perpendicularly to the substrate during the entire drying process. This implies that some alignment of the easy magnetization directions of the nanoparticles can be expected. The field induced magnetization for the dispersion at room temperature in a field of 35 mT is approximately 1/3 of the saturation magnetization, suggesting a modest degree of easy magnetization direction alignment.

2 Characterization of the nanoparticles

2.1 Powder X-ray diffraction

The powder X-ray diffraction pattern of the nanoparticles (Figure S1) was collected using a PANalytical X'Pert PRO with Cu-K α radiation ($\lambda = 1.5418 \text{ \AA}$) operating in transmission mode at 40 kV and 40 mA. A thin film of the nanoparticles was formed by successive additions of a concentrated dispersion onto a Kapton[®] foil window.

Powder silicon was used as a standard and the acquired powder pattern was refined using the Maud software package.¹ The pattern could be indexed according to the magnetite (Fe₃O₄) inverse spinel structure (ICSD no: 26410 Space group: *Fd-3m* (227)). The cell edge, *a* was found to be 8.353(1) \AA . This value is closer to the corresponding literature value for maghemite ($a_{\gamma\text{-Fe}_2\text{O}_3} = 8.34 \text{ \AA}$), than that of magnetite ($a_{\text{Fe}_3\text{O}_4} = 8.40 \text{ \AA}$).² Analysis of the isotropic peak width³ yielded a particle size of $D_{XRD} = 92(2) \text{ \AA}$. Furthermore, preliminary analysis of the X-ray diffractogram anisotropic peak widths using the so-called Popa rules⁴ suggests that there is slight elongation

along the $\langle 100 \rangle$ directions and relatively large strain on the $(h00)$ planes.

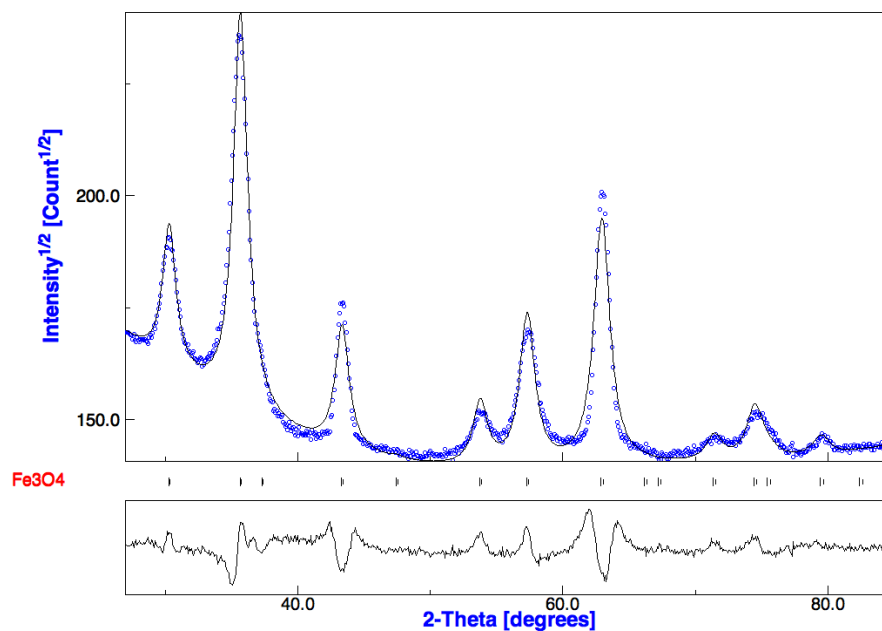


Figure S1: Experimental X-ray diffraction pattern (blue circles) and the corresponding isotropic Rietveld refinement (black line) of the nanoparticles. The reflections corresponding to Fe_3O_4 are indicated together with the difference spectrum (bottom graph).

2.2 Transmission electron microscopy

The nanoparticles were characterized using a JEOL JEM-2100 200 kV TEM (LaB₆, C_s=1.4 mm, point resolution=2.5 Å) by depositing a droplet of a dilute dispersion onto an ultrathin carbon-coated TEM grid (Ted Pella Inc).

A size distribution histogram was constructed by measuring the diameter of ≈ 400 nanoparticles. The images were collected on a Gatan SC1000 ORIUS camera (2004×1336 pixels) at 250 k× magnification. The image magnification was calibrated using the d_{220} spacing (2.96 Å from powder X-ray diffraction). A typical image and the fitted histogram is depicted in Figure S2. The histogram was fitted with a Gaussian distribution function

$$f(D) = -\frac{1}{\sigma\sqrt{2\pi}} \exp\left[-\frac{(D - \langle D \rangle)^2}{2\sigma^2}\right],$$

yielding an average particle diameter of $\langle D \rangle = 9.1$ nm and a standard deviation of $\sigma = 0.6$ nm.

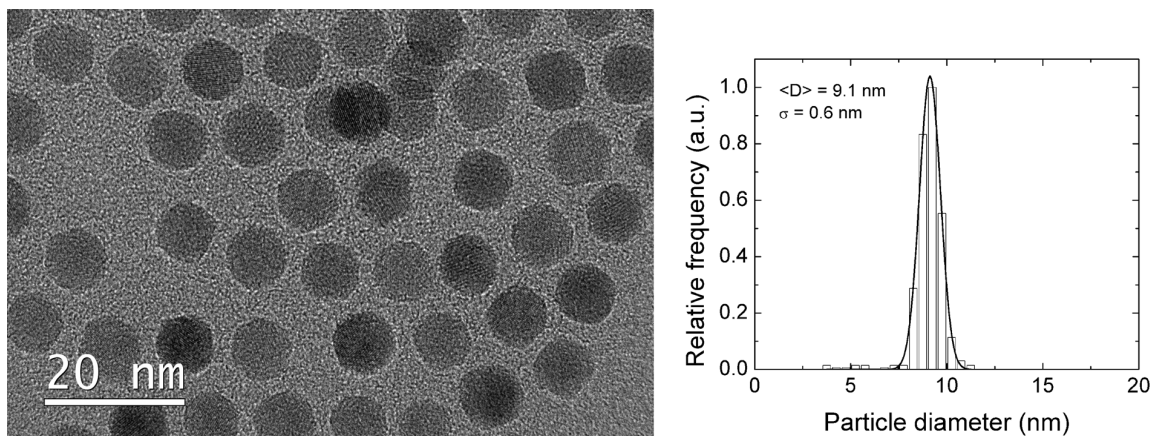


Figure S2: Transmission electron micrograph and statistical size distribution of the iron-oxide nanocrystals.

2.3 Small angle X-ray scattering

For the SAXS measurement, a rotating Cu anode lab source with a beam size of approximately 400 μm was used. The resolution of the instrument was 0.006 \AA^{-1} . The average size and size distribution were extracted by fitting the data with a spherical form factor, as shown in Figure S3. As the scattering profile displays only a form factor and no structure factor, we conclude that the concentration of the aggregated nanoparticles is below the detection limit of the measurement.

2.4 Dynamic light scattering

Dynamic light scattering (DLS) was performed using a Malvern ZetaSizer Nano ZS with a 4 mW He-Ne laser (633 nm). The viscosity of the solvent was used (cyclohexane, $\eta = 0.98$ cP), and the refractive index of the solvent and the particles was set to be 1.437 and 2.50, respectively. The volume distribution is shown in Figure S3 and has a maximum at $D_H = 14.0$ nm. This value is slightly larger than the expected value of $D_H = 13.1$ nm arising from a nanoparticle with an inorganic radius of 4.55 nm (see Figure S2) capped with a solvated layer of oleic acid with a

thickness of approximately 2 nm,⁵ thereby suggesting that the dispersion contains a small number of aggregates.

3 Characterization of the arrays

3.1 GISAXS characterization of the arrays

The reciprocal lattice constants (a^*/c^*) of a rhombohedral cell were obtained and averaged from all peak positions (Q_y/Q_z). The square root of the variance of these values was taken as the error. The real space lattice constants were then calculated using $a = \frac{4\pi}{a^*\sqrt{3}}$ and $c = \frac{2\pi}{c^*}$. The correlation lengths of the different arrays were obtained from the peak shapes of at least 6 peaks using a Lorentzian function to fit the peaks. The obtained peak widths at half maximum (γ) were corrected for the instrument resolution using $\gamma_{exp} = \gamma_{calc} - \gamma_{inst}$, where the subindices *exp*, *calc* and *inst* correspond to the experimental, calculated, and instrumental value, respectively. The correlation lengths were then taken as $2\pi/\gamma$ and are shown in the main text (Table 1). Note that due to beam-time limitations, the measurement of the medium sample was carried out on a laboratory setup. The thick sample was measured in both setups for cross-correlation purposes.

3.2 AFM characterization of the arrays

Atomic Force Microscopy (AFM) was used to determine the thickness and homogeneity of the arrays. The images shown in Figure S4 were acquired on a Veeco Bioscope 2 instrument, using a cantilever with a nominal resonant frequency of 75 kHz and a force constant of 3.5 N/m (Model: μ -masch NSC 18). In all the arrays, the absence of empty regions on the silicon wafer surface did not allow for a determination of their absolute thicknesses. The thin array is made of a few layers of nanoparticles. A $1 \times 1 \mu\text{m}^2$ scan showed a height difference in the arrays of ± 1 layer. The thickness calculated from the concentration of the droplet (25 nm) relates well with the apparent thickness on the AFM scans. The medium array is made of islands with a thickness of 50 to 80 nm,

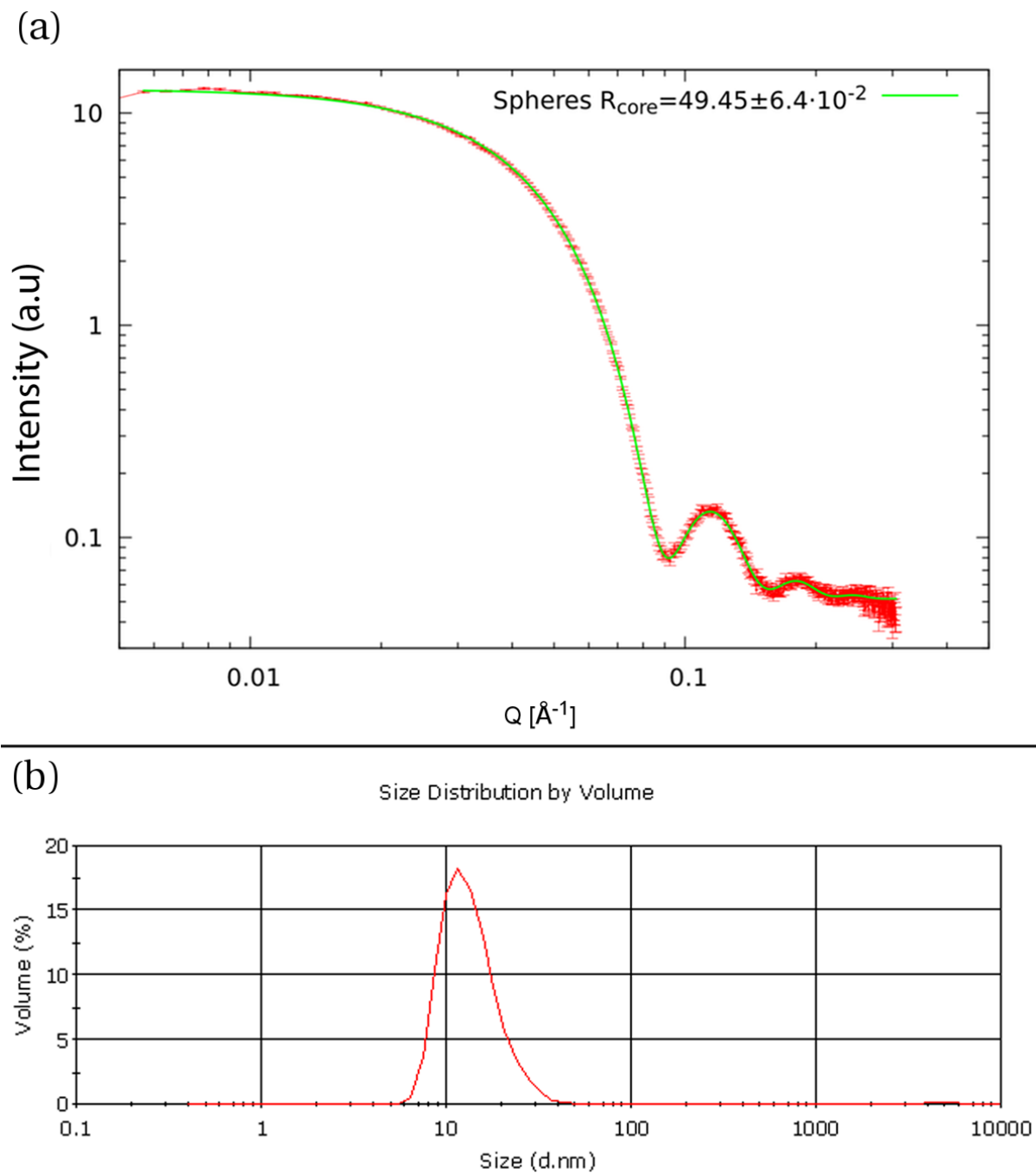


Figure S3: Investigation of the dispersion state of the dilute dispersion using scattering techniques. (a) SAXS profile of the 0.1 wt% dispersion with the corresponding fit using a spherical form factor. (b) Size distribution by volume obtained from DLS data of the same dispersion.

in good agreement with the expected thickness of 60 nm. Finally, the thick array is composed of bulk islands with a height in the μm range. Due to the roughness of this sample, it is not possible to approximate it as an array studied in the Monte Carlo simulations. Nevertheless the thick array is expected to have a magnetic behavior intermediate between an array with thickness 300 nm (expected thickness) and a bulk 3D array, which were both simulated.

4 Magnetic characterization

4.1 Magnetic relaxation time

In AC susceptibility experiments, the temperature dependence of the relaxation time (τ) for the nanoparticle magnetic moments can be derived from the freezing temperatures (T_f). This is done by identifying the experimental observation time $1/2\pi f$ as the relaxation time τ at T_f . Different approaches have been devised to extract the freezing temperatures. The most common way is to identify the frequency dependent cusp temperatures in χ' as the freezing temperatures. In another approach, the freezing temperatures are defined from the onset of dissipation, using a relation like $\chi'(T_f, \omega) = A \cdot \chi_{FC}(T_f)$ to define the onset of dissipation.⁶ In this work, we have used both the cusp temperature in χ' and the onset of dissipation, the latter with the constant $A = 0.95$, to extract T_f . A fit of the extracted freezing temperatures for the dilute dispersion to an Arrhenius law $\tau(T_f) = \tau_0 \exp(KV_p/T_f)$, where τ_0 is a microscopic relaxation time, yields unphysical values for both τ_0 and K . This is a clear signature of interparticle interactions. To account for dipole-dipole interactions between nanoparticles we used the Vogel-Fulcher (VF) law instead:⁷

$$\tau(T_f) = \tau_0 \exp\left(\frac{KV_p}{k_B(T_f - T_0)}\right), \quad (1)$$

where T_0 relates to the interparticle interactions. Using T_f defined from the cusp temperatures in χ' for the dispersion in the fitting, one obtains $K \approx 4.1 \times 10^4 \text{ J/m}^3$, a value that matches the value derived from χ' in the limit $T \rightarrow 0$ (see below). K -values of similar magnitude have been reported

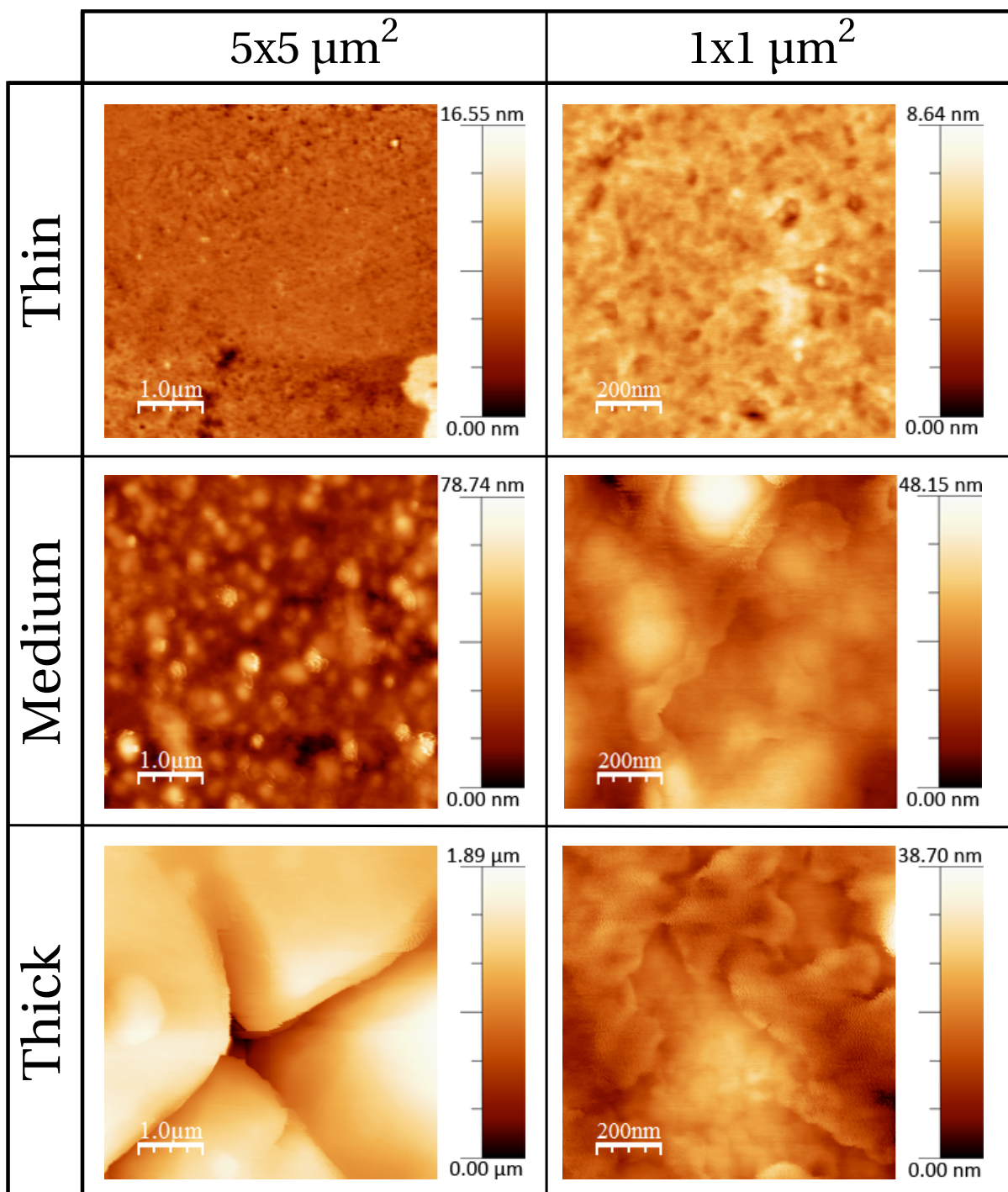


Figure S4: Large ($5 \times 5 \mu\text{m}^2$) and small ($1 \times 1 \mu\text{m}^2$) AFM micrographs of the thin, medium and thick arrays.

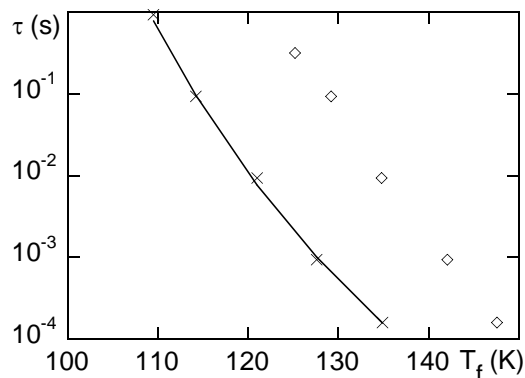


Figure S5: Relaxation time τ vs. freezing temperature T_f for the thick array (\diamond) and for the dispersion (\times) measured with a field amplitude of 0.32 kA/m, and at 0.17, 1.7, 17, 170 and 1000 Hz for the dispersion, and 0.5, 1.7, 17, 170 and 1000 Hz for the thick array. The solid line is a fit of the Vogel-Fulcher law to the result of the dispersion.

from other studies of maghemite nanoparticles.⁸ The anisotropy constant is one order of magnitude larger than the value measured for epitaxial single-crystal films and powders of γ -Fe₂O₃ suggesting that the anisotropy energy in the nanoparticles is dominated by contributions (e.g., strain induced) other than the magnetocrystalline anisotropy.^{9,10} However, the obtained value of $\tau_0 \approx 4 \times 10^{-14}$ is too small for magnetic nanoparticles. Using instead the freezing temperatures derived from the onset of dissipation, a more realistic value of $\tau_0 \approx 1 \times 10^{-11}$ was obtained together with an anisotropy constant $K \approx 4.1 \times 10^4$ J/m³. In both cases the extracted value of T_0 is in the range 60 – 65 K. It should be noted though that the uncertainties in the extracted values are large, partly because the AC susceptibility measurements were performed with a temperature resolution of 5 K. The freezing temperatures derived from the onset of dissipation relation are shown in Figure S5, together with the fit of the data for the dispersion to the VF law. The $\tau(T_f)$ data for the thick array was not accurate enough to render a fit to the VF law meaningful.

4.2 Temperature dependence of the magnetization

The temperature dependence of the nanoparticles magnetization was determined in two ways. The first method was measuring the magnetization versus field at different temperatures. The second method was to measure magnetization versus temperature measurements using an applied

field $H = 800$ kA/m. The result from the latter measurement (open symbols) performed on the nanoparticle paste is shown in Figure S6, together with a fit (solid line) of the experimental data to $M_s(T)/M_s(0) = 1 - BT^\beta$, with B and β as fitting parameters. The fit yields $\beta = 1.78 \pm 0.02$ and $B = 5.3 \pm 0.6 \times 10^{-6} \text{ K}^{-1.78}$.

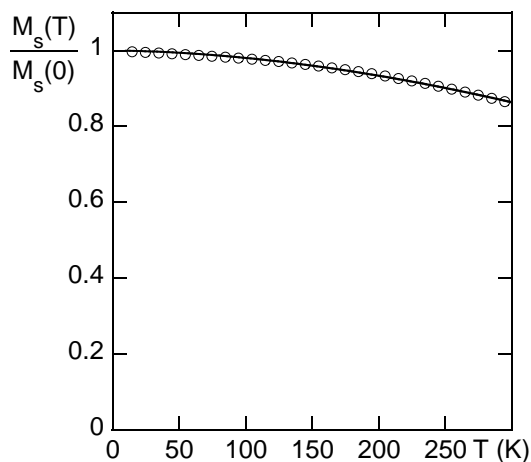


Figure S6: Magnetization versus temperature with an applied field $H = 800$ kA/m. The solid line is a fit of the experimental data to $M_s(T)/M_s(0) = 1 - BT^\beta$, with B and β as fitting parameters.

4.3 Temperature dependence of the susceptibility

The Curie-Weiss law provides an expression for the low-field susceptibility $\chi = C/(T - \alpha C)$. The Curie constant (C) exhibits a temperature dependence. This is because the magnetic moments of the nanoparticles are temperature dependent according to $C(T) = \mu_0 M_s^2(T) V_p / 3k_B$, where V_p is the volume of a particle. This yields Eq. (2) using a mean field approach with the dipolar interaction field given by $H_d = \alpha M$. M here being the field-induced magnetization and α is the mean-field constant; α is negative for antiferromagnetic coupling and positive for ferromagnetic coupling.

$$\frac{1}{\chi} = \frac{T - \alpha C(0)(1 - BT^\beta)^2}{C(0)(1 - BT^\beta)^2} \quad (2)$$

4.4 Exchange bias effect

Figure S7 displays the normalized magnetization M/M_s versus the magnetic field at $T = 10$ K for the thick array (solid line). The dashed curve shows the hysteresis loop displaced by the exchange bias field $H_{EB} = 6.4$ kA/m, in order to be symmetric around zero field. The exchange bias field is the same for all array samples, clearly showing that this effect is intrinsic to the nanoparticles and not due to the dipolar interactions in the arrays. The existence of intraparticle magnetic disorder associated with defective crystal structures would explain the exchange anisotropy of the particles, as well as the reduced value of M_s compared to the bulk value.¹¹ This could be manifested either as crystallographic defects in the nanoparticle core volume or as a defective surface layer. The origin of the exchange bias in single-phase particles will be discussed in an upcoming publication.

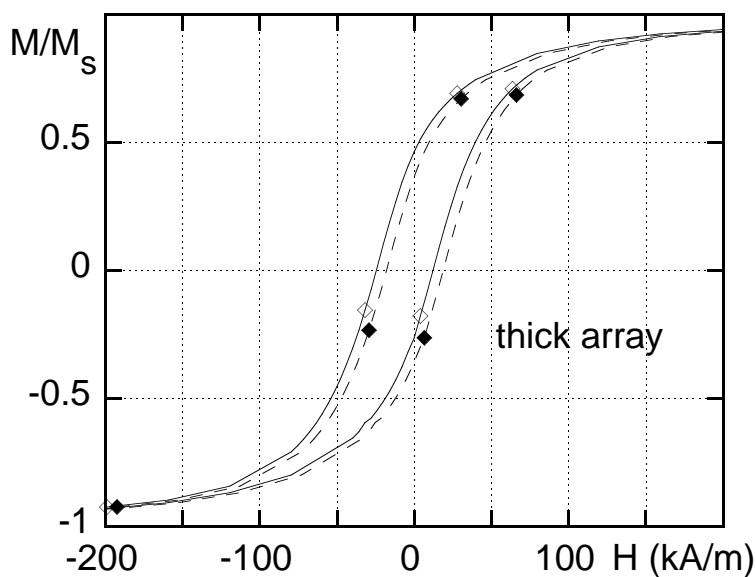


Figure S7: Magnetization M/M_s vs. magnetic field H for the thick array at $T = 10$ K. The solid lines (open symbols) correspond to the measured magnetization. The dashed curves (filled symbols) show the hysteresis loop when it has been displaced with H_{EB} to be symmetric around zero field.

4.5 Full hysteresis loops

The full hysteresis curves of the arrays and the dispersion can be seen in Figure S8, after correction for exchange bias effects.

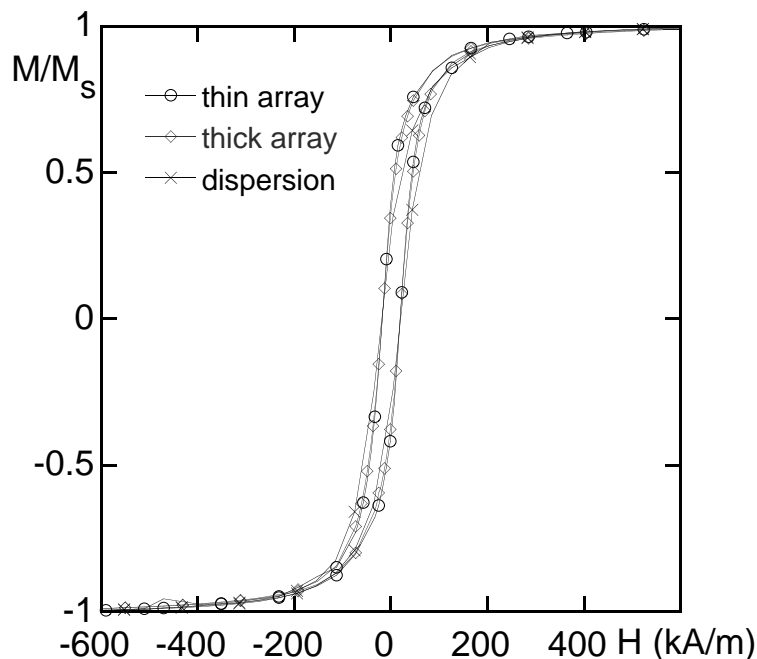


Figure S8: Full hysteresis loops for the dispersion (\times), the thin (\circ) and the thick (\diamond) arrays.

4.6 AC susceptibility measurements

AC magnetization versus temperature was investigated between 5 K and 250 K with an AC magnetic field amplitude of 0.32 kA/m and for frequencies in the range 0.17 – 1000 Hz. Figure S9 shows the in-phase component χ' of the AC susceptibility versus temperature for different frequencies of the AC magnetic field. The results in the figure were obtained from measurements on the thick array and the dispersion. The in-phase component of the AC susceptibility should approach a frequency independent value as the temperature $T \rightarrow 0$, corresponding to the intra-potential-well response of the particle magnetic moments χ_{\perp} ¹²

$$\chi_{\perp} = \frac{\mu_0 M_s^2(0)}{2K} \langle \sin^2(\theta) \rangle, \quad (3)$$

where K is the uniaxial anisotropy constant, θ is the angle between the magnetic field and the easy axis of magnetization and $\langle \sin^2(\theta) \rangle$ is averaged over the distribution of easy axis orientations. Since both the dispersion and the thick array approach very similar frequency independent values it is reasonable to adopt a random distribution of easy axis orientations, $\langle \sin^2(\theta) \rangle = 2/3$, for both

samples. The low temperature part (10 – 70 K) of the χ' -curves shown in Figure S9 (left figure) was fitted to a third order polynomial, yielding $\chi_{\perp} = 1.35 \pm 0.05$. Using the previously determined value for the saturation magnetization, a value of $K = 4.2 \pm 0.2 \times 10^4 \text{ J/m}^3$ can be extracted.

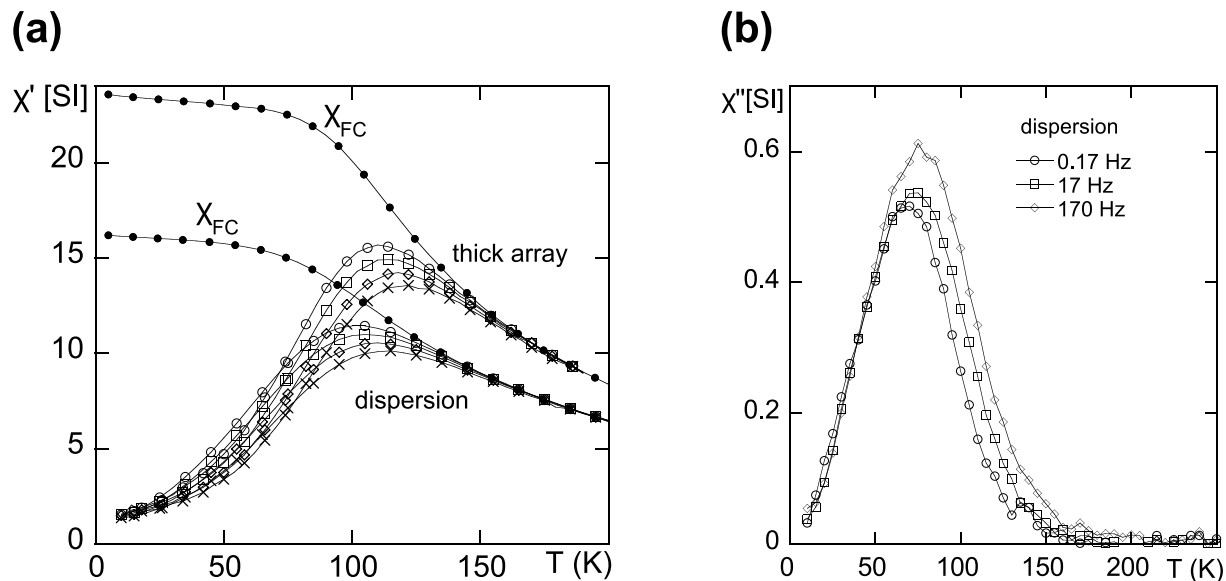


Figure S9: (a) In-phase component of the AC susceptibility χ' vs. temperature T for the thick array and for the dispersion. The different curves correspond to different frequencies of the AC magnetic field; 0.5 Hz, 1.7 Hz, 17 Hz, 170 Hz and 1 kHz for the thick array (top to bottom), and 0.17 Hz, 1.7 Hz, 17 Hz, 170 Hz and 1 kHz for the dispersion (top to bottom). The FC susceptibility χ_{FC} vs. temperature curves have been included to give the order of magnitude of the equilibrium susceptibility, and were obtained with a field of 0.4 kA/m. (b) Out-of-phase component of the AC susceptibility versus temperature for the dispersion. The different curves correspond to different frequencies of the AC field, with a field amplitude of 0.32 kA/m.

The thick array exhibits frequency dependent χ' -cusps at higher temperatures than the dispersion, thus indicating an increase of the relaxation times for the particle magnetic moments in the array due to dipolar couplings.

Figure S9 (right) shows the frequency dependence of the out-of-phase component of the AC susceptibility of the dispersion. The peak height of $\chi''(T)$ for the dispersion increases with increasing frequency. This trend is the opposite of the expected behavior for non-interacting nanoparticles.¹³ It indicates that the dynamics of this sample is influenced by weak interparticle interactions originating from the small nanoparticle aggregates mentioned above.⁶

4.7 Array thickness dependence of the non-equilibrium behavior

It is also interesting to compare the non-equilibrium behavior for the different nanoparticle arrays. Figure S10 shows the magnetic irreversibility $\chi_{\text{irr},n}$, defined as the difference between the FC and ZFC susceptibilities versus temperature, normalized with the difference measured at $T = 5$ K. Even though the effect is not large, it is still possible to conclude that the relaxation times for the particle arrays increase with increasing layer thickness.

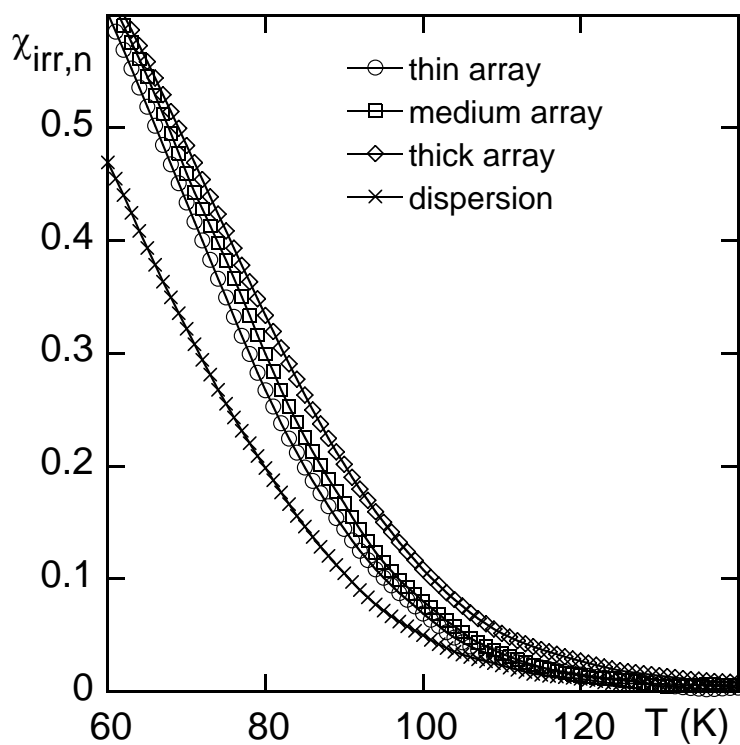


Figure S10: $\chi_{FC} - \chi_{ZFC}$ normalized with its value at $T = 5$ K vs. temperature for the three arrays, with a field amplitude of 0.8 kA/m. The corresponding result for the dispersion is included for comparison.

4.8 Onset of the non-equilibrium state

At temperatures slightly below 150 K, the susceptibility data does not correspond to a system at equilibrium. This is shown by the appearance of an out-of-phase component of the AC susceptibility. The results for the medium and thick arrays, as well as for the dispersion are shown in Figure S11. The onset of relaxation occurs at higher temperature for the nanoparticle arrays as compared to the dispersion. The temperature dependence of the out-of-phase component of the AC susceptibility for the thin array is similar to that of the other arrays, but has been left out from Figure S11 because of poor signal-to-noise ratio.

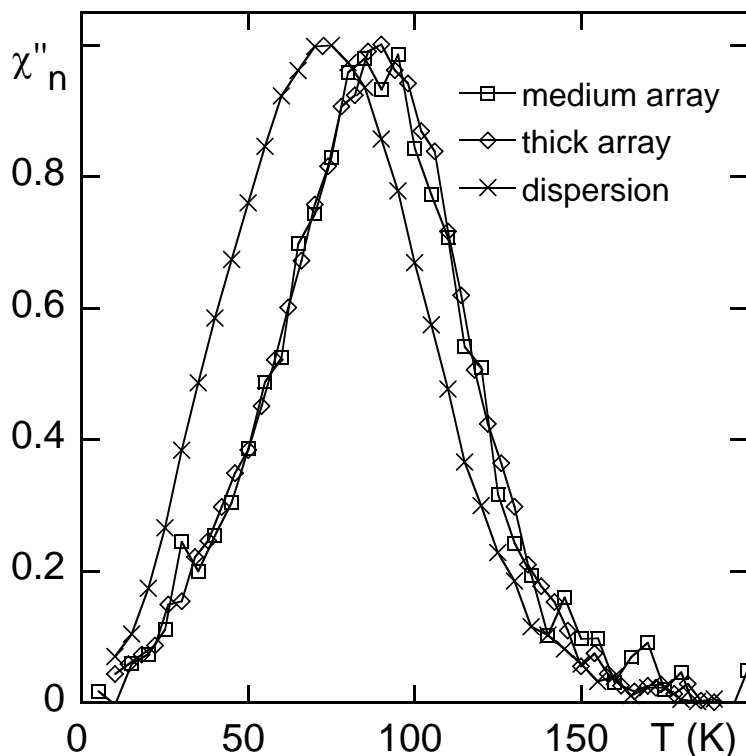


Figure S11: Out-of-phase component of the AC susceptibility normalized with its maximum value (χ''_n) versus temperature for the medium (\square) and thick (\diamond) arrays, and for the dispersion (\times). The amplitude and frequency of the AC magnetic field are 0.32 kA/m and 17 Hz, respectively.

5 Monte Carlo simulations

5.1 Description of the model system

The Monte Carlo simulations were performed on an ordered array of magnetic dipoles. Each particle is a single magnetic domain and contributes by its dipole moment to the magnetization.¹⁴ The array of dipoles is ordered in hexagonal dense layers parallel to the substrate and stacked in an *fcc* fashion, as shown in Figure 1(g). The number of close-packed layers in the simulated systems (3, 6 and 30) was chosen to match the thickness of the arrays assuming a full uniform coverage of the silicon wafer during the drop casting. A monolayer and a bulk array were simulated as well to explore the two limiting cases of this system. An external magnetic field \vec{H} is applied along the *x* direction, as shown in Figure S12.

The contributions of the external field \vec{H} (Zeeman energy), the magnetic anisotropy and the dipolar energy have been considered in the energy calculation (Eq. (4)).¹⁵

$$\hat{H} = \sum_i^{N_{box}} \left[-\mu_0 \vec{m}_i \cdot \vec{H} + \kappa \left(1 - \left(\frac{\vec{m}_i \cdot \hat{e}_i}{m_i} \right)^2 \right) + \frac{1}{2} \sum_{j, j \neq i}^{N_{box}} E_{ij} \right], \quad (4)$$

where each dipole *i* possesses a dipole moment \vec{m}_i . μ_0 is the permeability of free space and \hat{e}_i is a unit vector along the direction of easy magnetization, randomly chosen for each particle. We have used the expression for uniaxial anisotropy, where $\kappa = KV$ is the anisotropy energy per particle. The dipolar energy between two dipoles *i* and *j* is defined in Eq. (5).

$$E_{ij} = \frac{\mu_0}{4\pi} \left(\frac{\vec{m}_i \cdot \vec{m}_j - 3(\vec{m}_i \cdot \hat{n}_{ij})(\vec{m}_j \cdot \hat{n}_{ij})}{r_{ij}^3} \right), \quad (5)$$

where r_{ij} is the distance between the centres of the two particles and \hat{n}_{ij} is the unit vector connecting them. Direct and indirect exchange have been neglected since the particles are not in direct contact according to the GISAXS data.¹⁶

Periodic boundary conditions are applied in the *x* and *y* directions with the minimum image convention, and free boundary conditions on the top and bottom of the arrays. The dimensions of

the simulation boxes and the number of dipoles are given in Table SI. At the beginning of each simulation, the simulation box was filled with a distorted fcc array of particles, using the lattice parameters of the thick arrays from the GISAXS pattern (Table 1). $KV/k_B T \approx 4$ at $T = 300$ K for the iron-oxide nanoparticles studied in this work. Hence the degree of alignment of the particle easy axes during preparation of the arrays will be modest. Therefore, the easy magnetization direction for each particle was chosen randomly and remained fixed throughout each MC simulation. Dipolar interactions with particles within the simulation box are calculated by direct pairwise summation. The interactions with dipole moments outside the simulation box are evaluated by a mean-field approach, using a finite 2D array of images of the simulation box (Figure S12). The mean-field dipolar contributions are approximated as the total dipole moment in each (x, y) plane of the simulation box (parallel to the substrate). The dipolar interaction energy between the collective moment in each plane and their images outside the simulation box is calculated, and distributed uniformly over all the particles within the same plane. We used a cut-off distance of $2 \mu\text{m}$ in the x and y directions for the summation of the mean-field dipolar interaction energy. This procedure was not used for the simulation of the bulk array, which was based on direct pairwise summation with 3D periodic boundary conditions. The dispersion was simulated by turning off dipolar interactions.

Table SI: Dimensions and number of particles in the simulation box. The dimensions are given as a triplet along the x , y , and z axes defined in Figure S12.

Number of layers	Dimensions (nm)	Number of particles
1	121×105	100
3	$121 \times 105 \times 30$	300
6	$121 \times 105 \times 60$	600
30	$121 \times 105 \times 300$	3000
Bulk (∞)	$145 \times 137 \times 120$	2304

At the beginning of each simulation, the simulation box was filled with an *fcc* array of particles, using the lattice parameters of the thick arrays from the GISAXS pattern (Table 1). The easy magnetization direction for each particle was chosen randomly and remained fixed throughout each

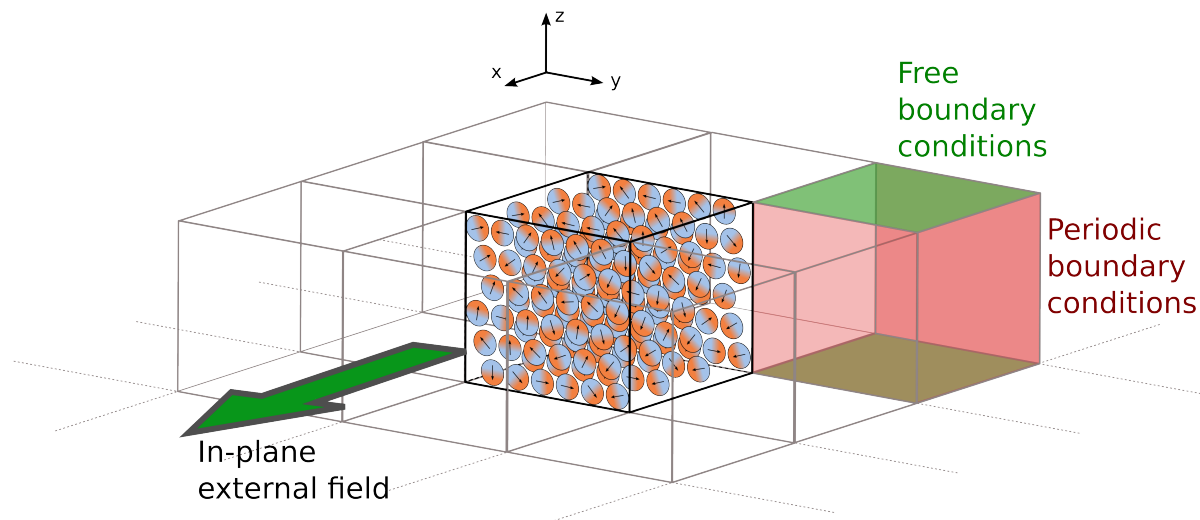


Figure S12: Model used to describe the arrays. The simulation box (black edges) is filled with randomly-oriented particles, whose easy axes are illustrated by the arrows. Periodic boundary conditions are applied on the faces perpendicular to the substrate. The top and bottom faces have free boundary conditions. The dipolar interactions are evaluated by direct pairwise summation within the central simulation box, using the minimum image convention. A mean-field approach (equivalent to a direct plane-wise summation) is then used to calculate the dipolar interactions in a finite 2D array of copies (grey edges) centered around the simulation box.

MC simulation. The temperature-dependent magnetic moment of the nanoparticles was calculated according to $m(T) = M_s(0)V_p \times (1 - 5.3 \times 10^{-6}T^{1.78})$ with $M_s(0) = 367$ kA/m.

At each step of the Monte Carlo algorithm, a particle is randomly picked in the simulation box and the direction of its dipole moment is randomly modified within a solid angle ΔS . The new orientation is accepted if it decreases the total energy (Eq. (4)), or with a probability of $e^{\frac{-\Delta \hat{H}}{k_B T}}$ if it increases the total energy ($\Delta \hat{H} > 0$) (Metropolis algorithm).¹⁷ The procedure is repeated as many times as the number of particles in the simulation box, which we call a big step. Each simulation consists of 10000 big steps. The magnetization along the direction of the external field is thermally averaged over the last 5000 big steps, and sampled every 10 steps. The magnetic energy after 5000 steps had converged within 95% of the extrapolated asymptotic value for an infinite number of big steps.

The procedure used for updating the directions of the magnetic dipoles followed the Solid Angle Restriction scheme.¹⁸⁻²⁰ The new direction of a magnetic moment was chosen at random

within the solid angle interval ΔS centered on the previous direction.²¹ The value of ΔS was regulated to maintain a probability of acceptance for the MC steps between 30 and 40 % throughout the simulations.

The standard error on the simulated ZFC data is defined as the standard deviation of the magnetic susceptibility divided by the square-root of the number of independent simulations (between 25 for the thick array up to 325 for the monolayer).

5.2 Observation of the 2D to 3D crossover

The formation of closed-circuit loops (vortex states) inside the films can be quantified using the vorticity, a vector field defined as the curl of the magnetic dipole moments ($\nabla \times \vec{m}$), using an approach borrowed from fluid dynamics. The magnetic moments are interpolated to a regular grid using a Gaussian radial basis function,^{22,23} and the vorticity vectors are calculated at each interpolated lattice position using the central differences method. 2D periodic boundary conditions are used in the x and y directions, while non-magnetic layers are appended below and above the array to represent free boundary conditions. 3D periodic boundary conditions are used to calculate the vorticity field in the bulk arrays.

The average orientation of the vorticity vectors is analyzed by calculating the x , y and z components of the vorticity field. Flux closure in the (x,y) plane results in a vorticity vector pointing out-of-plane in the z -direction. Therefore the vorticity field can be split into in-plane and out-of-plane components, calculated as the average root sum square of the vorticity along the x and y axes, $\langle V_{\text{out}} \rangle = \frac{1}{N_{\text{box}}} \sum (\sqrt{V_x^2 + V_y^2})$ for the out-of-plane component and as $\langle V_{\text{in}} \rangle = \frac{1}{N_{\text{box}}} \sum \sqrt{V_z^2}$ for the in-plane component of the vorticity field. The ratio of twice the squared in-plane contribution over the squared out-of-plane one $\frac{2\langle V_{\text{in}} \rangle^2}{\langle V_{\text{out}} \rangle^2}$ relates to the average orientation of the vortex states and is 1 for an isotropic distribution.

5.3 Field-dependent susceptibility

The in-plane ZFC curves have been measured and simulated under the influence of medium and strong external fields (1.6 kA/m and 8 kA/m, respectively), as shown in Figure S13. It can be seen in Figure S13 (a) that the susceptibility decreases with increasing field strength. This feature is reproduced in the simulated curves. The field dependence of the ZFC susceptibility is a result of two energies; the dipole-dipole interaction energy and the field energy. At low field, the field energy attempting to align the nanoparticle magnetic moments with the applied field can induce a comparably large magnetization with the assistance of the dipolar interaction field favoring parallel alignment of the nanoparticle magnetic moments. A stronger dipolar interaction field (larger α value) yields a larger susceptibility, which explains the larger susceptibility of the thin array. With increasing external magnetic field, deviations from a linear response will become more and more apparent (the rate by which the magnetization increases with increasing field will decrease) and the measured susceptibility decreases. Since the low field susceptibility is larger for the thin array compared to that of the thick array, a non-linear response will show up at smaller fields for the thin array and the ZFC susceptibility for this array will therefore also exhibit a stronger field dependence in the investigated field range.

The measured magnetic behavior is qualitatively reproduced in the simulated ZFC data. It was not possible to simulate ZFC data at low external field (0.4 kA/m) because the statistical error on the data points increases with decreasing field. Assuming that the response of the dipole array to the external field is linear, the number of dipoles contributing to the net magnetization of the array is proportional to the field. Thus if the field strength is decreased by one order of magnitude, the size of the statistical ensemble of magnetic states should be one order of magnitude larger to maintain the precision. The computation cost at low field is thus high.

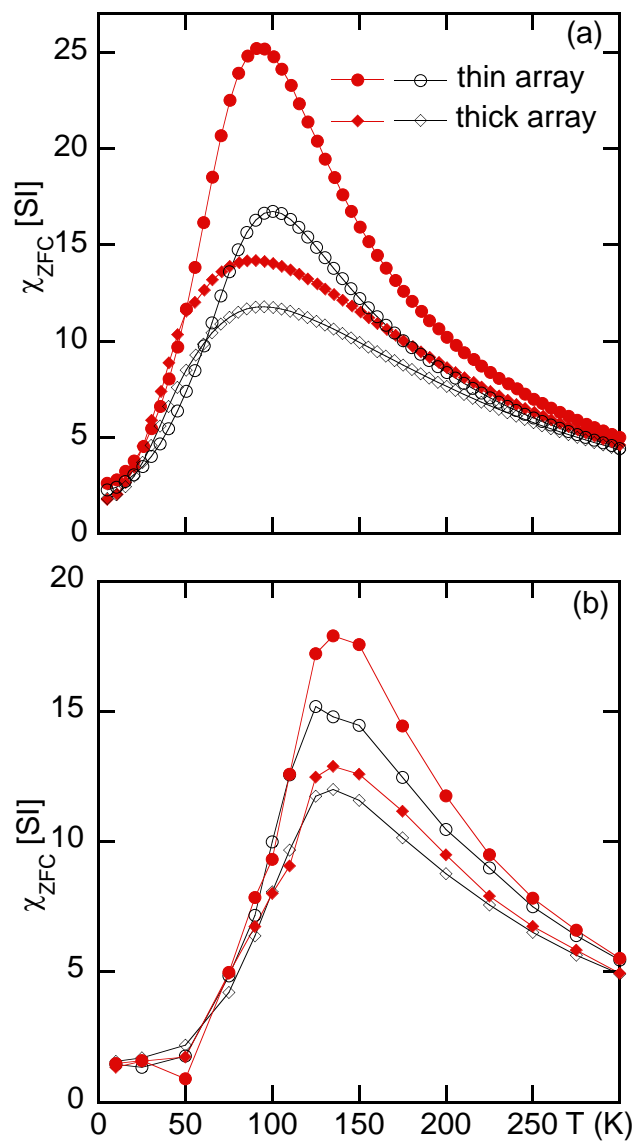


Figure S13: Field-dependence of the ZFC magnetization for the thin (\circ) and thick (\diamond) arrays, at medium (full symbols) and high (open symbols) external field (1.6 kA/m and 8 kA/m, respectively). (a) Experimental curves. (b) Simulated curves.

References

1. Lutterotti, L. Maud - Materials Analysis using Diffraction. 2011; <http://www.ing.unitn.it/~maud/>.
2. Cornell, R. M.; Schwertmann, U. *The iron oxides: structure, properties, reactions, occurrences, and uses*; Wiley-VCH, 2003; p 664.
3. Lutterotti, L.; Scardi, P. Simultaneous structure and size-strain refinement by the Rietveld method. *J. Appl. Crystallogr.* **1990**, *23*, 246–252.
4. Popa, N. The (hkl) Dependence of Diffraction-Line Broadening Caused by Strain and Size for all Laue Groups in Rietveld Refinement. *J. Appl. Cryst.* **1998**, *31*, 176–180.
5. Tadmor, R.; Rosensweig, R. E.; Frey, J.; Klein, J. Resolving the Puzzle of Ferrofluid Dispersants. *Langmuir* **2000**, *16*, 9117–9120.
6. Hansen, M. F.; Jönsson, P. E.; Nordblad, P.; Svedlindh, P. Critical dynamics of an interacting magnetic nanoparticle system. *J. Phys.: Condens. Matter* **2002**, *14*, 4901.
7. Shtrikman, S.; Wohlfarth, E. P. The theory of the Vogel-Fulcher law of spin glasses. *Phys. Lett. A* **1981**, *85*, 467 – 470.
8. Rebbouh, L.; Hermann, R. P.; Grandjean, F.; Hyeon, T.; An, K.; Amato, A.; Long, G. J. ^{57}Fe Mössbauer spectral and muon spin relaxation study of the magnetodynamics of monodispersed $\gamma\text{-Fe}_2\text{O}_3$ nanoparticles. *Phys. Rev. B* **2007**, *76*, 174422.
9. Vassiliou, J. K.; Mehrotra, V.; Russell, M. W.; Giannelis, E. P.; McMichael, R. D.; Shull, R. D.; Ziolo, R. F. Magnetic and optical properties of $\gamma\text{-Fe}_2\text{O}_3$ nanocrystals. *Journal of Applied Physics* **1993**, *73*, 5109–5116.
10. Takei, H.; Chiba, S. Vacancy Ordering in Epitaxially-Grown Single Crystals of $\gamma\text{-Fe}_2\text{O}_3$. *Journal of the Physical Society of Japan* **1966**, *21*, 1255–1263.

11. Batlle, X.; Pérez, N.; Guardia, P.; Iglesias, O.; Labarta, A.; Bartolomé, F.; García, L. M.; Bartolomé, J.; Roca, A. G.; Morales, M. P. et al. Magnetic nanoparticles with bulklike properties (invited). *J. Appl. Phys.* **2011**, *109*, 07B524.
12. Svedlindh, P.; Jonsson, T.; García-Palacios, J. L. Intra-potential-well contribution to the AC susceptibility of a noninteracting nano-sized magnetic particle system. *J. Magn. Magn. Mater.* **1997**, *169*, 323 – 334.
13. Raikher, Y. L.; Stepanov, V. I. Linear and cubic dynamic susceptibilities of superparamagnetic fine particles. *Phys. Rev. B* **1997**, *55*, 15005–15017.
14. Stoner, E. C.; Wohlfarth, E. P. A Mechanism of Magnetic Hysteresis in Heterogeneous Alloys. *Philos. Trans. Roy. Soc. London* **1948**, *240*, 599–642.
15. Arias, P. R.; Altbir, D.; Bahiana, M. Geometric aspects of the dipolar interaction in lattices of small particles. *J. Phys.: Condens. Matter* **2005**, *17*, 1625–1633.
16. Altbir, D.; d’Albuquerque e Castro, J.; Vargas, P. Magnetic coupling in metallic granular systems. *Phys. Rev. B* **1996**, *54*, R6823–R6826.
17. Metropolis, N.; Rosenbluth, A. W.; Rosenbluth, M. N.; Teller, A. H.; Teller, E. Equation of State Calculations by Fast Computing Machines. *J. Chem. Phys.* **1953**, *21*, 1087–1092.
18. Dimitrov, D.; Wysin, G. M. Magnetic properties of superparamagnetic particles by a Monte Carlo method. *Phys. Rev. B* **1996**, *54*, 9237–9241.
19. Pereira Nunes, J.; Bahiana, M.; Bastos, C. Magnetization curves as probes of Monte Carlo simulation of nonequilibrium states. *Phys. Rev. E* **2004**, *69*, 056703.
20. Trohidou, K. N.; Vasilakaki, M. In *Applications of Monte Carlo Method in Science and Engineering*; Mordechai, S., Ed.; InTech, 2011; Chapter 20.
21. Karney, C. F. F. Quaternions in molecular modeling. *J. Mol. Graph. Model.* **2007**, *25*, 595–604.

22. Press, W. H.; Teukolsky, S. A.; Vetterling, W. T.; Flannery, B. P. *Numerical Recipes 3rd Edition: The Art of Scientific Computing*, 3rd ed.; Cambridge University Press, 2007; Chapter 3, pp 110–154.
23. Verestóy, J.; Chetverikov, D.; Nagy, M. Digital PIV: a Challenge for Feature Based Tracking. 2012; <http://visual.ipan.sztaki.hu/pivweb/>.